

Evidence of Stress Control on Dissolution Cavity Growth Along Heterogeneous Field-Scale Fractures From Coupled Hydro-Mechanical-Chemical Modeling

Jiang, Chuanyin; Wang, Xiaoguang; Lei, Qinghua; Liu, Lijun; Song, Guofeng; Jourde, Hervé

DOI

[10.1029/2024JB029901](https://doi.org/10.1029/2024JB029901)

Publication date

2025

Document Version

Final published version

Published in

Journal of Geophysical Research: Solid Earth

Citation (APA)

Jiang, C., Wang, X., Lei, Q., Liu, L., Song, G., & Jourde, H. (2025). Evidence of Stress Control on Dissolution Cavity Growth Along Heterogeneous Field-Scale Fractures From Coupled Hydro-Mechanical-Chemical Modeling. *Journal of Geophysical Research: Solid Earth*, 130(2), Article e2024JB029901. <https://doi.org/10.1029/2024JB029901>

Important note

To cite this publication, please use the final published version (if applicable).
Please check the document version above.

Copyright

Other than for strictly personal use, it is not permitted to download, forward or distribute the text or part of it, without the consent of the author(s) and/or copyright holder(s), unless the work is under an open content license such as Creative Commons.

Takedown policy

Please contact us and provide details if you believe this document breaches copyrights.
We will remove access to the work immediately and investigate your claim.

JGR Solid Earth

RESEARCH ARTICLE

10.1029/2024JB029901

Key Points:

- A new coupled HMC model is developed to capture stress-dependent dissolution along a field-scale heterogeneous fracture
- Stress promotes branched and localized dissolution, which may cause a qualitative change in the dissolution regime
- Wormholes initiate from remote stiffer regions and converge toward the inlet for a dissolution regime with a high penetration length

Supporting Information:

Supporting Information may be found in the online version of this article.

Correspondence to:

X. Wang,
wangxiaoguang@cdut.edu.cn

Citation:

Jiang, C., Wang, X., Lei, Q., Liu, L., Song, G., & Jourde, H. (2025). Evidence of stress control on dissolution cavity growth along heterogeneous field-scale fractures from coupled hydro-mechanical-chemical modeling. *Journal of Geophysical Research: Solid Earth*, 130, e2024JB029901. <https://doi.org/10.1029/2024JB029901>

Received 11 JUL 2024

Accepted 12 FEB 2025

Author Contributions:

Conceptualization: Xiaoguang Wang
Formal analysis: Chuanyin Jiang, Xiaoguang Wang
Methodology: Chuanyin Jiang, Qinghua Lei, Lijun Liu, Guofeng Song
Resources: Hervé Jourde
Software: Qinghua Lei
Supervision: Hervé Jourde
Writing – original draft: Chuanyin Jiang
Writing – review & editing: Xiaoguang Wang, Qinghua Lei, Lijun Liu, Guofeng Song, Hervé Jourde

© 2025. The Author(s).

This is an open access article under the terms of the [Creative Commons Attribution-NonCommercial-NoDerivs License](#), which permits use and distribution in any medium, provided the original work is properly cited, the use is non-commercial and no modifications or adaptations are made.

Evidence of Stress Control on Dissolution Cavity Growth Along Heterogeneous Field-Scale Fractures From Coupled Hydro-Mechanical-Chemical Modeling

Chuanyin Jiang^{1,2}, Xiaoguang Wang^{3,4,5} , Qinghua Lei² , Lijun Liu^{3,5}, Guofeng Song⁶, and Hervé Jourde¹

¹HydroSciences Montpellier (HSM), University of Montpellier, CNRS, IRD, Montpellier, France, ²Department of Earth Sciences, Uppsala University, Uppsala, Sweden, ³State Key Laboratory of Geohazard Prevention and Geoenvironment Protection, Chengdu University of Technology, Chengdu, China, ⁴Faculty of Land Resource Engineering, Kunming University of Science and Technology, Kunming, China, ⁵Tianfu Yongxing Laboratory, Chengdu, China, ⁶Department of Geoscience and Engineering, Delft University of Technology, Delft, The Netherlands

Abstract We develop a new coupled hydro-mechanical-chemical (HMC) model to investigate the stress-controlled evolution of dissolution cavities along a hectometer-scale heterogeneous fracture. The fracture is conceptualized to consist of numerous patches associated with spatially-variable, stress and dissolution-dependent local stiffnesses and apertures. We consider the complete coupling relationships among mechanical deformation, fluid flow, and chemical dissolution within the fracture. More specifically, our model captures non-linear fracture deformational responses and their consequences on localized flow pattern and dissolutional aperture growth, as well as the feedback of dissolution to mechanical weakening and stress redistribution. We elucidate how geomechanical processes affect the aperture and flow patterns and the formation of small to large dissolution cavities. Our simulation results show that stress retards the permeability increase with the extent of retardation positively related to a dimensionless penetration length l_p' . Stress induces the splitting of the dissolution front, promoting localized flow and branched dissolution. At low l_p' (wormhole dissolution regime), stress also promotes the sustained growth of dissolution branches. Hence, there is no apparent increase in global flow heterogeneity. At high l_p' , stress transitions the system from uniform dissolution into wormhole formation. Wormholes initiate from remote stiffer regions and converge toward the inlet. Our results have important implications for understanding various dissolution phenomena in subsurface fractured rocks, ranging from karstification to reservoir acidization.

Plain Language Summary Understanding how fractures dissolve is of great importance for various geoscience and geoenvironment problems, such as karst formation, hydrocarbon extraction, groundwater management, and geothermal development. However, subsurface fractures are inevitably influenced by the associated stress condition. The interplay among stress, heterogeneity, flow, and dissolution in field-scale fractures still has not been well understood so far. Here, we develop a new numerical model that couples fracture dissolution with mechanical deformation and fluid flow to investigate this problem. We elucidate how fracture dissolution affects the stress re-distribution, which, in turn, controls the fracture opening and the flow organization as well as the dissolution process. The simulation results show that stress can slow the fracture opening due to dissolution and lead to more branched dissolution pathways. Under conditions of high flow rates or less soluble rock, localized dissolution is favored instead of uniform dissolution under the application of stress. Additionally, the localized dissolution pathways develop from the outlet. This study provides mechanistic insights for some karst morphologies observed in nature and also has important implications for relevant engineering applications.

1. Introduction

Fracture dissolution as a ubiquitous phenomenon in the Earth's crust is highly relevant to a variety of geoscience and geoenvironment problems, ranging from karst genesis and reservoir acidization to groundwater remediation and geothermal development. The mechanisms of hydro-chemical (HC) coupling in fracture dissolution have been extensively investigated through laboratory experiments (e.g., Detwiler et al., 2003; Wang et al., 2022) and numerical simulations (e.g., Cheung & Rajaram, 2002; Hanna & Rajaram, 1998; Starchenko & Ladd, 2018), where the dissolution patterns are governed by the Damköhler number (Da) comparing reaction and advection

rates. A low Da (slow reaction rate) tends to generate uniform dissolution throughout the fracture, while a high Da (fast reaction rate) promotes the instability of dissolution fronts, leading to the formation of so-called “wormholes” (Szymczak & Ladd, 2009). The penetration length l_p is also an important indicator of the instability of the dissolution front (Szymczak & Ladd, 2011): the dissolution front is always unstable to induce wormholes if the fracture length is sufficiently larger than l_p ; conversely, uniform dissolution is favored if it is close to l_p .

Fractures in geological systems are inevitably subject to in-situ stress loading, exhibiting non-linear permeability reduction under normal compaction (Laura J Pyrak-Nolte & Nolte, 2016; Petrovitch et al., 2013). Therein, fracture stiffness is an effective parameter to capture the interactive roles of void spaces and asperities in governing the coupled hydro-mechanical (HM) behavior of rough fractures (Pyrak-Nolte & Morris, 2000). Dissolution processes along stressed fractures involve hydro-mechanical-chemical (HMC) coupling, as revealed by previous experimental and numerical studies. For example, laboratory experiments based on rock cores showed that dissolution leads to mechanical weakening (reduction in rock stiffness), which in turn impacts the pore deformation and impedes permeability enhancement (e.g., Clark & Vanorio, 2016; Detwiler, 2008; Elkhoury et al., 2013). A recent reactive transport modeling study for micro-scale stressed porous media also illuminated the competing effects between dissolutional enlargement and mechanical compaction, which involves a two-way mechanical-chemical (MC) coupling (Roded et al., 2018). Nevertheless, for rough fractures, most existing models only considered the one-way MC coupling mechanism where the dissolutional enlargement is added directly to the reduced aperture that is induced by mechanical deformation (e.g., Pandey et al., 2018; Wang et al., 2021; Xu et al., 2021) or pressure solution (e.g., Ogata et al., 2018; Yasuhara et al., 2006, 2015). Some other models regarding dissolution in stressed rough fractures mainly focused on the pore scale effect and explicitly describe the deformation of local pore space and the alteration in the contact zones of asperities (e.g., Ameli et al., 2014; Lang et al., 2015).

The long-term dissolution processes in stressed rough fractures at a field scale remain poorly understood. Recently, a few reservoir-scale models incorporating two-way MC coupling have been applied to assess the relative importance of poroelastic, thermoelastic, and chemical effects in geothermal development (Salimzadeh & Nick, 2019; Song et al., 2022). However, an idealized condition of smooth fracture surfaces was assumed in these studies without considering the spatial variability of local fracture apertures and the stress dependency of local fracture stiffnesses. A significant knowledge gap, therefore, exists regarding the interplay of aperture heterogeneity and stress state in the dissolving field-scale heterogeneous fractures. Moreover, the abovementioned geothermal-related modeling only focused on high- l_p dissolution scenarios (artificial flow conditions and silica reservoirs). It is important to develop a comprehensive understanding of stress-controlled fracture dissolution mechanisms covering the full spectrum from low- l_p (wormhole) to high- l_p (uniform) regimes. Note that the term “wormhole” hereafter represents the formation and evolution of localized and branched dissolution conduits at the field scale like karstic conduits/caves in fractured carbonate terrains.

Here, we present a new coupled HMC model to investigate stress-controlled dissolution along a two-dimensional (2D) heterogeneous field-scale fracture embedded in a three-dimensional (3D) rock block subject to normal stress loading. The model considers the complete coupling relationships among stress, flow, and dissolution within the large heterogeneous fracture. It can also capture such important effects as stress-dependent aperture variation, non-linear stiffness evolution, heterogeneity-induced flow channeling, and dissolution-induced mechanical weakening. The results obtained from this study enhance our mechanistic understanding of the emergence of diverse dissolution patterns in geological systems.

2. Methodology

2.1. Model Description

2.1.1. Model Conceptualization

Our model adopts a lower-dimensional representation (Figure 1) to capture the coupled HMC processes in a field-scale fracture of a size reaching up to 100 m. The fracture is discretized into a large number of local patches with sizes of ~ 1 m (Figure 1b), where each patch corresponds to a representative elementary area (REA) (Figure 1c). The behavior of each local patch (formed by numerous asperities) is described by relevant constitutive laws and effective properties. In other words, the local patch size defines the support scale of our model, below which the microscopic details will not be explicitly considered. However, the effects of microscopic asperity interactions

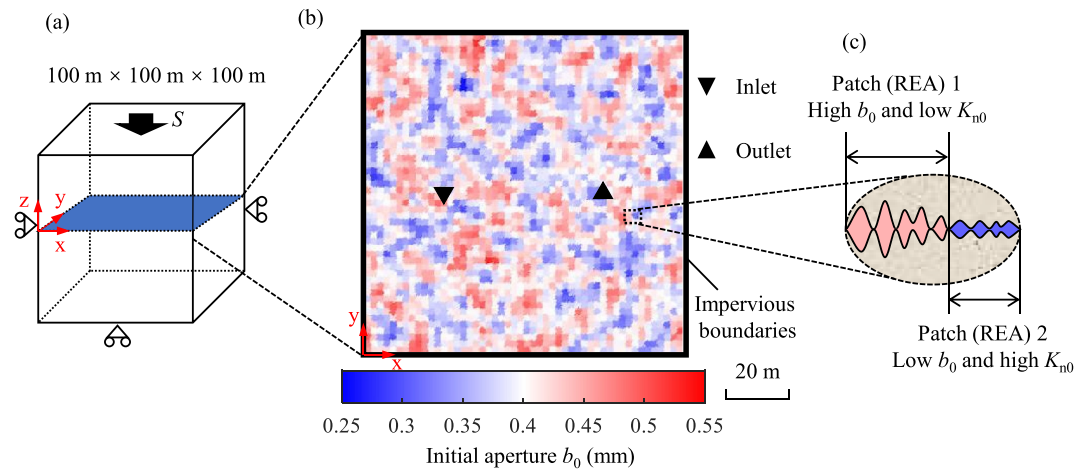


Figure 1. (a) Model setup for simulating dissolution processes in a stressed hectometer-scale fracture with (b) a spatially variable initial aperture field (each local patch represents a representative elementary area, REA); (c) Schematics of roughness profiles of local opposing fracture walls below the scale of REA patches. Note that the roughness profiles as shown in (c) are not explicitly represented in the model shown in (b) but their effects are implicitly modeled in (b). For example, the red patch with a high initial aperture b_0 in (b) corresponds to the red section in (c) with a larger surface roughness and a lower initial stiffness K_{n0} , while the blue patch in (b) with a lower aperture b_0 represents a smoother roughness profile in (c) with a higher K_{n0} .

can still be implicitly captured through the prescribed constitutive laws (e.g., stress-aperture relationship) and effective properties (e.g., aperture, stiffness) at each REA. This effective medium-type treatment, based on an assumption that the fracture size is much beyond the REA scale, allows us to parsimoniously model the important mesoscopic interactions among many local fracture patches that drive the emergence of stress-dependent dissolution phenomena at the large scale. Thus, our model is analogous to the conventional stochastic continuum models (Neuman, 1987) where a representative elementary volume (REV) is assumed at the grid block scale (Neuman, 1987; Xia et al., 2016). Our modeling framework is therefore conceptually different from the previous micromechanical models (e.g., Ameli et al., 2014; Lang et al., 2015), which explicitly represent asperity contacts that are below the REA scale. Hence, a key difference between our model and the micromechanical models lies in the scale of investigation, whether beyond or below the REA scale.

Our model captures the following important stress-dissolution processes. Initially, each REA within the fracture exhibits a spatially variable initial aperture b_0 , resulting from the variation of local roughness conditions of the two opposing fracture walls (Figures 1b and 1c). This aperture variability is also accompanied with a heterogeneous distribution of local initial normal stiffness K_{n0} across the fracture. After the application of stress but before any dissolution, all the REA patches enter a “contact mode” but exhibit different degrees of closure depending on their local stiffnesses. Note that the contact mode in this study refers to the compressed state of a local fracture patch, which is subject to a normal compressive stress but has a non-zero aperture, because the opposing patch walls are supported by many asperities. In the contact mode, the aperture b of each REA patch exhibits a non-linear stiffness response under increased stress (Bandis et al., 1983; Rutqvist et al., 2002). This constitutive law implicitly reflects an increase in the contact area between the local opposing walls. Subsequently, as dissolution progresses, the aperture of the local REA patch increases (driven by an interplay of stress and dissolution), while the stiffness decreases, reflecting a decreased local contact area. Therefore, our model could implicitly capture the effect of contact area reduction due to lateral dissolution at the asperity scale, by modeling the changes of local properties like aperture and stiffness. In contrast, the micromechanical models (e.g., Ameli et al., 2014; Pyrak-Nolte & Nolte, 2016) only considered vertical dissolution processes. After long-term dissolution within the fracture, the aperture of a local REA may exceed its initial value, indicating that the local opposing patch walls are fully detached and a dissolution cavity is locally formed. At this stage, the local compressive stress diminishes to zero, and the local patch is in an “open mode” of zero contact area, with the previously afforded load redistributed to the nearby undissolved REA patches (in a contact mode) that would be subject to stress concentration and aperture decrease.

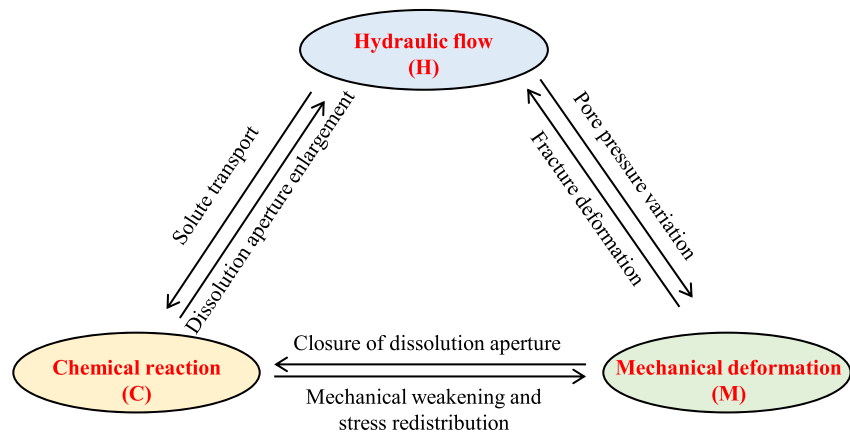


Figure 2. Coupled processes of hydraulic flow, mechanical deformation, and chemical reaction captured in our HMC model.

2.1.2. Model Setup and Features

We consider a 3D rock cube ($100\text{ m} \times 100\text{ m} \times 100\text{ m}$) bisected centrally by a 2D horizontal discontinuity and vertically subject to confining stress (Figure 1a). This discontinuity may represent the typical scenario of confined bedding planes or laterally extended discontinuities where dissolution features prevalently develop in nature (Cheung & Rajaram, 2002; Palmer, 1991). The fracture has a spatially variable initial aperture field where we discretize the domain into a grid of REA patches (Figure 1b). The initial aperture field follows a Gaussian distribution with a self-affine spatial correlation (e.g., Brown, 1995; de Dreuzy et al., 2012). Here, we assume the mean, standard deviation, and correlation length as 0.4 mm, 0.04 mm, and 12.5 m, respectively. The generated aperture field consists of 50×50 patches (Figure 1b). Instead of analyzing the directional flow condition seen in most micro-scale experimental or numerical studies (e.g., Detwiler, 2008; Roded et al., 2018), we study the radial flow scenario, which is more prevalent in field applications (e.g., Roded et al., 2023). Here, concentrated inlet and outlet points are placed at (25 m, 50 m) and (75 m, 50 m) to represent natural sinkhole recharge and spring discharge or artificial injection and production wells (Figure 1b).

The novelty of our coupled HMC model is reflected by its unique capability of simultaneously capturing (a) the multiscale nature of dissolution processes over both the time domain (from early-stage initiation to long-term evolution) and spatial domain (from small-scale mechanical and transport heterogeneity to large-scale dissolution cavity formation), and (b) the multiphysics nature of dissolution behaviors driven by the coupling among HMC processes (Figure 2). Each local REA patch of the fracture has two mechanical states: (a) contact mode and (b) opening mode. In the contact mode, the local two opposing fracture walls touch with each other, with the deformation (closure behavior) governed by the local stress and stiffness. Although in contact, local areas could remain hydraulically conductive, with the conductivity varying as a function of fracture closure obeying the cubic law (Witherspoon et al., 1980). Dissolution results in aperture enlargement, causing mechanical weakening (stiffness reduction) and stress redistribution, which in turn impact the fracture closure and conductivity. If the dissolution-induced enlargement exceeds compaction-induced closure, the fracture transitions from contact into opening mode. In the opening mode, the local fracture walls are fully detached from each other, forming a dissolution cavity that could also deform in response to stress. Note that the mechanical weakening in this study refers to the loss of stiffness caused by the detachment of local fracture surfaces. We do not consider the effect of deterioration of the rock matrix after water immersion (Steiger et al., 2011; Wong et al., 2016) here. Given the lack of relevant field-scale experimental data, we verify our geomechanical calculation of cavity deformation by comparing it with an explicit representation model (see Appendix A). This verification confirms the validity of our lower-dimensional model and illuminates the phenomenon of local stress redistribution due to dissolution-induced changes in fracture surface geometry.

2.2. Governing Equations

We assume the rock matrix surrounding the high-conductivity fracture is impermeable (Hyman et al., 2022) and calculate flow and transport within the 2D fracture plane. The steady-state mass conservation equation for the

single-phase flow of incompressible fluid, incorporating the Poiseuille laminar flow model, is expressed as (Hanna & Rajaram, 1998):

$$\nabla \cdot (b\mathbf{v}) = 0, \mathbf{v} = -\frac{b^2}{12\mu}\nabla p, \quad (1)$$

where b is the local fracture aperture, \mathbf{v} is the velocity vector, μ is the fluid dynamic viscosity, and p is the pressure.

We assume the concentration field instantly equilibrates in each time step, associated with a time-varying aperture field driven by dissolution and deformation (Roded et al., 2018). This assumption is reasonable since the time scale of aperture alteration is much larger than that of ion concentration change (Hanna & Rajaram, 1998). Thus, the steady-state reactive transport equation is written as:

$$\nabla(b\mathbf{v}c) - \nabla \cdot (bD \cdot \nabla c) = 2R(c), \quad (2)$$

where c is the dissolved-ion concentration, D is the diffusion coefficient, and $2R(c)$ is the local reactive flux with a factor of two representing the contributions from the two opposing fracture walls. According to extensive previous numerical studies on incipient karstification (e.g., Dreybrodt & Gabrovšek, 2019; Szymczak & Ladd, 2011), we assume that the effective reaction kinetics are mainly related to the mechanical aperture of fractures, regardless of whether the fracture surfaces are in contact or not. This means that the dissolution rate gradually transitions from surface reaction-limited to diffusion-limited as the aperture increases (Szymczak & Ladd, 2011). Here, linear reaction kinetics, with an effective rate coefficient λ_{eff} , are used, as higher-order kinetics have been demonstrated to be inessential in 2D dissolution scenarios (Szymczak & Ladd, 2011). We compute $R(c)$ as:

$$R(c) = \lambda_{\text{eff}}(c_{\text{eq}} - c), \lambda_{\text{eff}} = \frac{\lambda}{1 + \frac{2\lambda b}{D \cdot Sh}}, \quad (3)$$

where c_{eq} is the equilibrium concentration, λ is the reaction rate constant, and Sh is the Sherwood number. Then, the aperture growth due to chemical dissolution is updated as:

$$c_{\text{sol}} \frac{db_c}{dt} = 2R(c), \quad (4)$$

where c_{sol} is the molar concentration of soluble material.

The 3D rock matrix is involved in mechanical computation which solves the following quasi-static momentum equilibrium equation:

$$\nabla \cdot \boldsymbol{\sigma} + \mathbf{F} = 0, \quad (5)$$

where $\boldsymbol{\sigma} = \mathbf{C} : \boldsymbol{\varepsilon}$ is the stress tensor, \mathbf{C} is the elasticity tensor, $\boldsymbol{\varepsilon} = (\nabla \mathbf{u} + \nabla^T \mathbf{u})/2$ is the strain tensor, \mathbf{u} is the displacement vector, and \mathbf{F} is the body force vector. Note that the poroelastic effect in the rock matrix is excluded as flow is solely confined within the fracture plane. Hydraulic pressure-related tractions are applied to the fracture walls as Neumann boundaries to the rock matrix (L. Liu et al., 2021):

$$\begin{aligned} \boldsymbol{\sigma} \cdot \mathbf{n}_f^+ &= -p\mathbf{I} \cdot \mathbf{n}_f^+ - \mathbf{t}_f^+ \\ \boldsymbol{\sigma} \cdot \mathbf{n}_f^- &= -p\mathbf{I} \cdot \mathbf{n}_f^- - \mathbf{t}_f^-, \end{aligned} \quad (6)$$

where \mathbf{n}_f is the unit normal vector, \mathbf{t}_f is the traction, and the superscripts '+' and '-' denote the two opposing fracture walls with $\mathbf{n}_f^+ = -\mathbf{n}_f^-$ and $\mathbf{t}_f^+ = -\mathbf{t}_f^-$. Note that the Biot coefficient for the fracture is set as 1.0. \mathbf{t}_f depends on the normal differential displacement b_d of the two opposing fracture walls given as:

$$b_d = (\mathbf{u}^+ - \mathbf{u}^-) \cdot \mathbf{n}_f^+, \quad (7)$$

where \mathbf{u}^+ and \mathbf{u}^- are the displacements of the upper and lower walls, respectively. If $b_d > 0$, the fracture is in an opening mode where the two faces are separated with zero tractions; otherwise, it is in a contact mode where the two faces are in contact with non-zero tractions such that b_d of a non-positive value defines the normal closure. The mechanical aperture b_m is then calculated as the summation of the initial aperture b_0 and the closure b_d . Extensive numerical and experimental observations have reported the presence of a non-linear relationship between normal closure (or permeability) and normal stress, where the fracture stiffness increases under the enhanced normal compaction (e.g., Bandis et al., 1983; Rutqvist et al., 2002). Here, we employ a fracture stiffness-aperture relationship established based on experimental results of a wide range of natural/artificial fractures and validated against an elastic-plastic contact model (Li et al., 2021):

$$K_n = \frac{\alpha \cdot E \cdot \text{RSD} \cdot b_{\text{ref}}}{b_h^2}, \quad (8)$$

where K_n is the effective normal stiffness, b_h is the hydraulic aperture, E is the elastic modulus of the rock matrix, RSD is the relative standard deviation of the local mechanical aperture, α is a dimensionless scaling factor with a value of 0.003, and b_{ref} is a reference aperture taking a value of 0.5 mm. This relationship has been demonstrated to be valid for the effective medium regime (typically when $b_h > 0.03$ mm). Also, in the effective medium regime, the hydraulic aperture b_h is found to be roughly equal to the mechanical aperture b_m (Li et al., 2021). Thus, Equation 8 can be approximately rewritten as:

$$K_n = \frac{\alpha \cdot E \cdot \text{RSD} \cdot b_{\text{ref}}}{b_m^2}. \quad (9)$$

Here, we consider the first-order effect of RSD assuming $\text{RSD} \approx 0.8$ (Li et al., 2021) so that the numerator of Equation 9 becomes a constant. By introducing $\eta = \alpha \cdot E \cdot \text{RSD} \cdot b_{\text{ref}}$ and recalling the definition of stiffness, Equation 9 is then written as:

$$K_n = -\frac{\partial \sigma'_n}{\partial b_m} = \frac{\eta}{b_m^2}, \quad (10)$$

where $\sigma'_n = \sigma_n - p$ is the effective normal stress corresponding to the normal component of traction \mathbf{t}_f . Integrating Equation 10 with $b_m = b_0$ when $\sigma'_n = 0$ yields:

$$b_m = b_0 + b_d = \left(\frac{1}{b_0} + \frac{\sigma'_n}{\eta} \right)^{-1}. \quad (11)$$

Here, we focus on the compaction-controlled fracture closure behavior, while the shear dilation effect (Jiang, Wang, Zhang, et al., 2022; Lei & Barton, 2022) is beyond the scope of the present study.

The aperture growth due to chemical dissolution, that is, Equation 4, is implicitly introduced as gaps in the fracture (Salimzadeh & Nick, 2019). In other words, the dissolution-induced aperture enlargement is treated as the separation of the opposing fracture walls, such that Equation 7 is rewritten as:

$$b_d = b_c + (\mathbf{u}^+ - \mathbf{u}^-) \cdot \mathbf{n}_f^+. \quad (12)$$

Due to the dissolution-induced aperture enlargement (i.e., dissolution gap), adjacent undissolved areas carry more load, experiencing more closure, and becoming stiffer, compared to dissolved areas. Contrarily, dissolved areas exhibit lower stiffnesses, leading to dissolution-induced mechanical weakening. In Appendix A, we present a systematic verification of this mechanical model and also demonstrate how the presence of cavities leads to the redistribution of local stresses.

Table 1
Parameters for the Coupled Hydro-Mechanical-Chemical Simulation

Parameters	Symbols	Values	Units
<i>Water</i>			
Dynamic viscosity	μ	1×10^{-3}	Pa·s
Density	ρ_f	1,000	kg/m ³
Reaction rate constant	λ	2.5×10^{-7}	m/s
Inlet concentration	c_{in}	0	mol/m ³
Sherwood number	Sh	8	—
Equilibrium concentration	c_{eq}	2	mol/m ³
Diffusion coefficient	D	1×10^{-9}	m ² /s
<i>Rock matrix</i>			
Young's modulus	E	30	GPa
Poisson's ratio	ν	0.25	—
Density	ρ_s	2,700	kg/m ³
Molar concentration	c_{sol}	2.7×10^4	mol/m ³
<i>Fracture</i>			
Initial aperture	b_0	0.25~0.55	mm
Effective normal stiffness	K_n	Variable	MPa/mm

The local stress S_c is then determined by Equation 11 based on the remaining gap, that is, the final differential displacement as defined by Equation 12, in each iteration of the calculation:

$$S_c = \sigma'_n = \begin{cases} \frac{\eta}{b_0 + b_d} - \frac{\eta}{b_0} & b_d \leq 0 \\ 0 & b_d > 0 \end{cases} \quad (13)$$

When the entire system reaches mechanical equilibrium, the final aperture b is updated as the final differential displacement following:

$$b = b_m = b_0 + b_d. \quad (14)$$

2.3. Model Parameterization

In the simulation, the outlet maintains a constant hydraulic pressure p_{out} while the inlet has a fixed flow rate Q_{in} and dissolved-ion concentration c_{in} . All the outer boundaries of the fracture are impervious to water. We subtract the outlet pressure p_{out} from both the external load and the pressure field. Thus, $p_{out(new)}$ becomes 0 and the external stress applied to the top boundary equals the effective stress S , equivalent to a simplified homogeneous pore pressure p_{out} considered in the rock matrix. Roller boundary conditions are specified for the other outer boundaries of the system, such that only normal compression to the fracture is considered while the shearing effect is negligible.

For other mechanical and transport properties, typical parameter values for carbonates undergoing dissolution induced by CO₂-rich water (Lei et al., 2017; Szymczak & Ladd, 2011) are employed (Table 1). To encompass both natural and artificial flow scenarios, we examine flow rates Q_{in} spanning three orders of magnitude (10^{-5} , 10^{-4} , and 10^{-3} m³/s), corresponding to initial pressure gradients ranging from approximately 0.01 to 1 m/m. Dissolution rates λ being 10 times higher or lower than the default value 2.5×10^{-7} m/s are also investigated, representing rock with higher or lower solubility, respectively.

The coupled HMC model is numerically solved using the finite element method (Jiang, Wang, Pu, & Jourde, 2022; L. Liu et al., 2021). Detailed verifications of the mechanical calculation and coupled HC simulation can be found in Appendix A and our previous work (Jiang, Wang, Pu, & Jourde, 2022). The numerical simulation runs in two stages: (a) model initialization to attain a mechanical equilibrium under prescribed stress loading through a ramp function and (b) model calculation of coupled HMC processes. Compared to the aperture field, a finer unstructured mesh with a maximum element size of $L/75$ (L is the domain size) is used to discretize the fracture to accurately capture the dissolution patterns and their evolution. The mesh in regions adjacent to the inlet and outlet is refined to a minimum element size of $L/1000$. The rock block is further discretized into five layers through a sweep method that exponentially increases the layer thickness (by a factor of 20) from the fracture surface to the outer boundaries. To ensure numerical convergence and stability, we utilize an implicit self-adaptive stepping method, constrained by a maximum time step of 0.1 years. A sequential coupling framework is adopted wherein fluid flow, reactive transport, chemical dissolution, and mechanical equilibration are sequentially solved in each iteration. Iterations proceed until the relative error falls below the tolerance threshold, after which the next time step is triggered. If a convergence cannot be attained, the time step is automatically halved and the iterations are re-executed. Simulations are terminated when the ratio of equivalent permeability κ for the region between the inlet and outlet to its initial value κ_0 reaches 100 (Roded et al., 2018), that is, the inlet pressure drops by 100 times.

2.4. Dimensionless Quantities

We define the following dimensionless quantities:

$$b' = \frac{b}{b_0}, K'_n = \frac{K_n}{K_{n0}}, S'_c = \frac{S_c}{S}, c' = \frac{c}{c_{eq}}, q' = \frac{ql}{Q_{in}}, \quad (15)$$

where \bar{b}_0 and \bar{K}_{n0} are the mean initial aperture and normal stiffness, S is the applied effective compressive stress, q is the local flow rate ($q = vb$), and l is the distance between the inlet and outlet. We also define PV as the injected fluid volume normalized by the initial pore volume of the fracture, that is, $PV = Q_{in}t/(\bar{b}_0L^2)$. PV_{BT} means the breakthrough volume of the injected fluid to achieve $\kappa/\kappa_0 = 100$. In addition, a dimensionless penetration length l_p' is defined to identify the dissolution regime:

$$l_p' = \frac{\bar{q}_0}{2\lambda l}, \quad (16)$$

where \bar{q}_0 is the mean initial flow rate along the straight line (length l) connecting the inlet and outlet. Then, $\bar{q}_0/(2\lambda)$ represents the mean initial penetration length along the connecting line (Szymczak & Ladd, 2011). Under a zero stress condition, if l_p' is very small (e.g., close to 0), the initial penetration length is distant from the outlet, leading to an unstable dissolution front and wormhole formation; if $l_p' > 1$, uniform dissolution is favored (Szymczak & Ladd, 2011). However, the control of l_p' in stressed fractures remains unexplored and will be examined in this study. With the explored Q_{in} and λ , the dimensionless penetration length l_p' in this paper ranges from ~ 0.02 to ~ 2 , covering scenarios from wormhole formation to uniform dissolution. We take the cases with the median inlet flow rate $Q_{in} = Q$ (10^{-4} m³/s) and a default dissolution rate $\lambda = 2.5 \times 10^{-7}$ m/s as the reference- l_p' case (with $l_p' \approx 0.2$). Increasing the flow rate to $10Q$ or decreasing the dissolution rate to $\lambda/10$ represents high- l_p' cases (with $l_p' \approx 2$), while $Q/10$ or 10λ corresponds to low- l_p' cases (with $l_p' \approx 0.02$).

The correlation dimension D_2 can be used to quantify the aperture heterogeneity (Jiang, Wang, Pu, & Jourde, 2022) and flow localization (X. Wang et al., 2017) along the fracture plane, which is computed as (Bonnet et al., 2001):

$$D_2 = \lim_{r \rightarrow 0} \frac{\log \sum_{i=1}^N (P_i)^2}{\log r}, \quad (17)$$

where P_i is the proportion of the local aperture or flow rate integrated over the i th square box of size r to that over the entire surface; N is the total number of square boxes; D_2 is calculated based on a 20×20 grid superimposed on the fracture. $D_2 = 2$ signifies a uniform field and a lower D_2 means a stronger heterogeneity.

3. Results

3.1. Effect of Normal Compressive Stress

Figure 3 shows the spatio-temporal evolutions of aperture b' and concentration c' for the reference- l_p' case with zero stress loading ($S = 0$ MPa), that is, involving solely HC coupling (Movie S1). Figure 5 summarizes the evolutions of the equivalent permeability ratio κ/κ_0 and final dissolution patterns at PV_{BT} for various cases. Initially, a radial dissolution front emerges. Under the positive feedback loop between flow and dissolution, the dissolution front progressively converges into a preferential pathway straightly connecting the inlet and outlet. When PV exceeds 1,000, the dissolution front arrives at the outlet (Figure 3g), resulting in a rapid increase of κ/κ_0 (Figure 5a). When PV approximates 3,500, the permeability reaches the target value of $\kappa/\kappa_0 = 100$.

In contrast, a markedly different dissolution behavior occurs under non-zero stress ($S = 30$ MPa), where HMC coupling dominates. In addition to aperture and concentration fields, Figure 4 further shows the evolutions of local stress S_c' and normal stiffness K_n' (Movie S2). When PV approaches 3,500, the dissolution front maintains its initial radial shape (Figure 4e) as the dissolution-induced aperture enlargement (i.e., gap) is closed by the strong normal compression. The local stress in the dissolution region is reduced but does not fall to zero (Figure 4i). Consequently, the final aperture enlargement is less pronounced (Figure 4a), accompanied by a subtle localized weakening in stiffness (Figure 4m). As dissolution progresses ($PV \approx 15,000$), the gap cannot be fully closed, leading to the initiation of a large dissolution cavity (Figure 4b). Also, the dissolution front starts to show disturbances. However, instead of rapidly converging in one direction, the dissolution front appears to develop a flower-like pattern (Figure 4f). This is attributed to the fact that the region in an open mode (with $S_c' = 0$) forces the adjacent regions to carry the extra normal compression load, resulting in localized stress concentrations (Figure 4j). Then, the highly elevated local stress leads to aperture reduction and further compaction (evidenced by increased stiffness, Figure 4n), splitting the dissolution front into multiple petals. When $PV \approx 27,200$, the dissolution front progressively evolves into a ramiform pattern (Figure 4g), characterized by a dominant branch

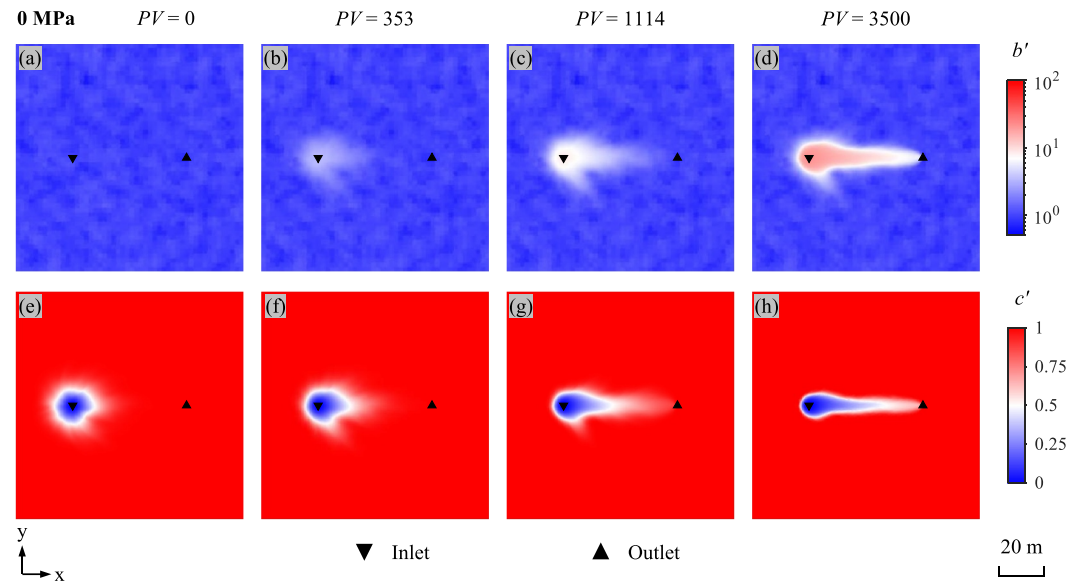


Figure 3. Spatio-temporal evolutions of aperture b' and concentration c' for the reference- l_p' case ($l_p' \approx 0.2$) with zero compressive stress $S = 0$ MPa.

along the central streamline and several distinct secondary branches. When $PV \approx 77,080$, breakthrough occurs as the unsaturated fluid concentrates in the central preferential branch (Figure 4h). The ramiform pattern becomes more pronounced with multiple sub-branches at the tips (Figures 4d–4l and 4p).

Various stress magnitudes are further examined (Figures 5c–5f). As S decreases, the secondary branches in the ramiform structure become less pronounced. However, even at low S , the stress-controlled dissolution pattern remains distinct from the zero-stress case. The former exhibits more tortuous pathways. In addition, normal compression substantially delays the breakthrough (Figure 5a). Due to stress suppression, the dissolution region remains in a contact mode, causing a slow increase in permeability at the beginning. When some local fracture surfaces transition into an opening mode, an abrupt rise in κ/κ_0 occurs, followed by a subsequent gradual increase. Normal compressive load not only prolongs the stagnation of flow field evolution but also greatly retards the subsequent flow focusing (see Fig. S1 in Supporting Information S1 for further details on the probability density function of local flow rates).

3.2. Effect of Penetration Length

The effect of the penetration length l_p' is examined by varying the inlet flow rate (Figures 5g–5j) or the dissolution rate (Fig. S2 in Supporting Information S1). When l_p' is small ($l_p' \approx 0.02$) under $S = 0$ MPa, a single narrow wormhole develops, predominantly following the low-resistance pathway meandering through the system (Figure 5g). When S is elevated to 30 MPa, the wormhole changes its direction during propagation, accompanied by the emergence of several distinct secondary branches (Figure 5h).

In contrast, for a high l_p' ($l_p' \approx 2$) under $S = 0$ MPa, uniform dissolution occurs, forming a teardrop-shaped front (Figure 5i). Similar to the low- l_p' case, more injected fluid (PV) is required to achieve $\kappa/\kappa_0 = 100$, compared to the reference- l_p' case (dash-dotted lines in Figure 5b). This indicates the highest dissolution efficiency corresponding to a moderate flow rate. In the high- l_p' regime, the evolution of κ/κ_0 exhibits a nearly linear trend due to uniform dissolution, distinct from the wormhole-dominated dissolution, which shows a dramatic increase of κ/κ_0 during breakthrough (Figure 5b).

However, for the high- l_p' case with $S = 30$ MPa, a notably distinct dissolution pattern emerges (Figure 5j). We present the spatial and temporal evolution of the two high- l_p' cases to elucidate the underlying mechanism (Figure 6, Movie S3 and Movie S4). Because of the high l_p' , the dissolution front has already reached the outlet from the beginning. When $S = 0$ MPa, the dissolution process appears relatively straightforward: the dissolution front exhibits a non-uniform pattern initially (Figure 6e) due to the aperture heterogeneity (Figure 6a), and

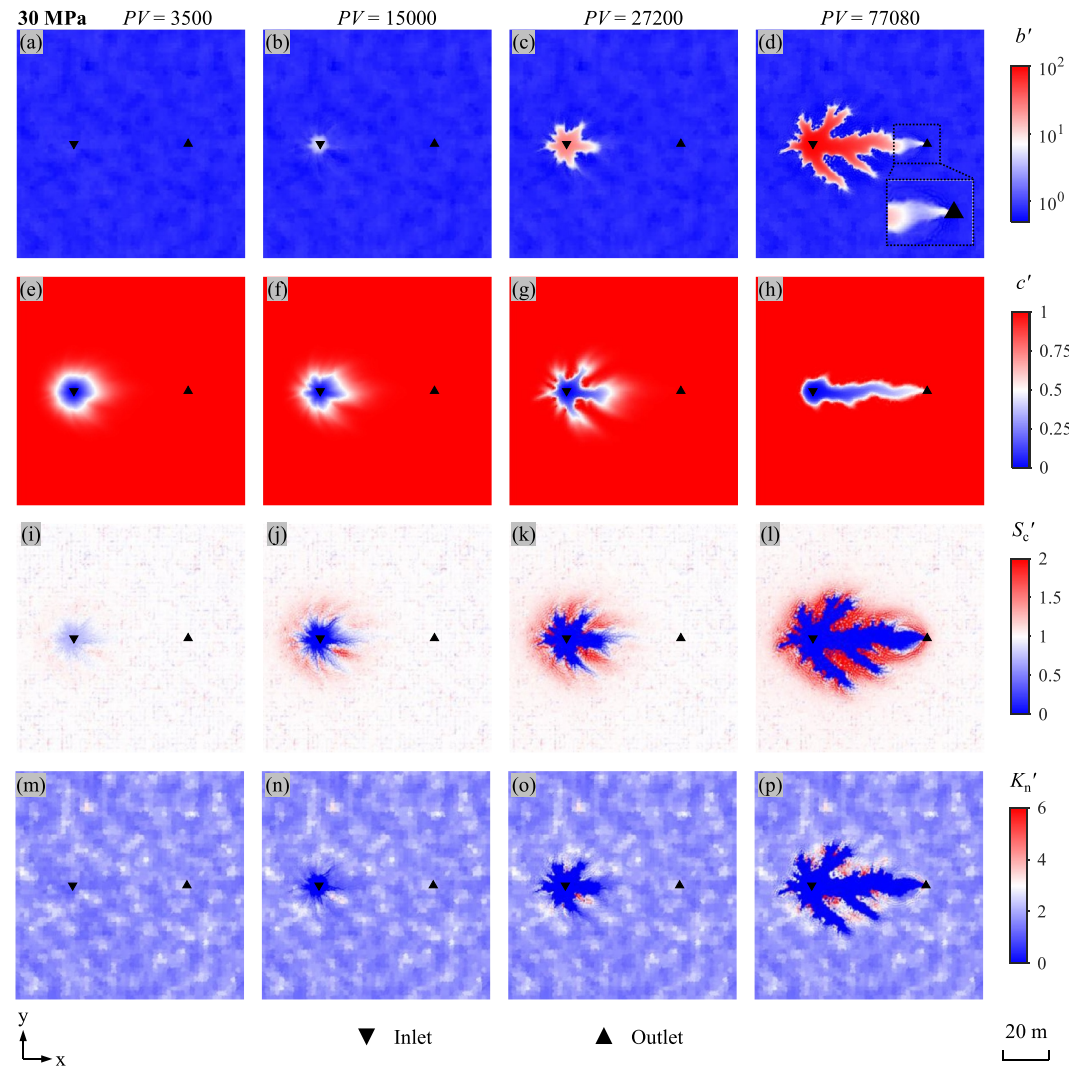


Figure 4. Spatio-temporal evolutions of aperture b' , concentration c' , local stress S_c' , and normal stiffness K_n' for the reference- l_p' case ($l_p' \approx 0.2$) with an effective normal compressive load $S = 30$ MPa.

subsequently evolves into a uniform teardrop-like pattern driven by the positive feedback loop between flow and dissolution. Contrarily, at $S = 30$ MPa, the dissolution front remains stable even under substantial PV (Figure 6m). Interestingly, in contrast to the cases with lower l_p' , a significant fracture opening initiates from the outlet (Figure 6i). This phenomenon is attributed to the convergent shape of the dissolution front: near the outlet, dissolution primarily occurs in the left region, while the rest remains undissolved and consistently bears the compression load (Figure 6q). Consequently, the dissolving channel near the outlet opens more compared to the one near the inlet, which experiences extensive dissolution and reclosure. A similar phenomenon is also observed in the reference- l_p' scenario when the dissolution front reaches the outlet (see zoomed-in view of Figure 4d). Subsequently, at $PV \approx 315,600$, the dissolving conduit progresses toward the inlet (Figure 6j), resulting in the retreat of the dissolution front. It is worth noting that the dissolution front near the inlet is progressively split into several localized channels by the local stress concentrations (Figures 6n and 6r), in contrast with the homogeneous pattern under $S = 0$ MPa. As PV increases, the separated channels begin to greatly widen from the tips of the dissolution front (Figure 6k) because the compacted regions between them bear the compression load (Figure 6s). Finally, the dissolving pathways originating from the remote stiffer regions converge toward the inlet, forming a large dissolution chamber connected with several localized narrow conduits (Figure 6l), distinct from the

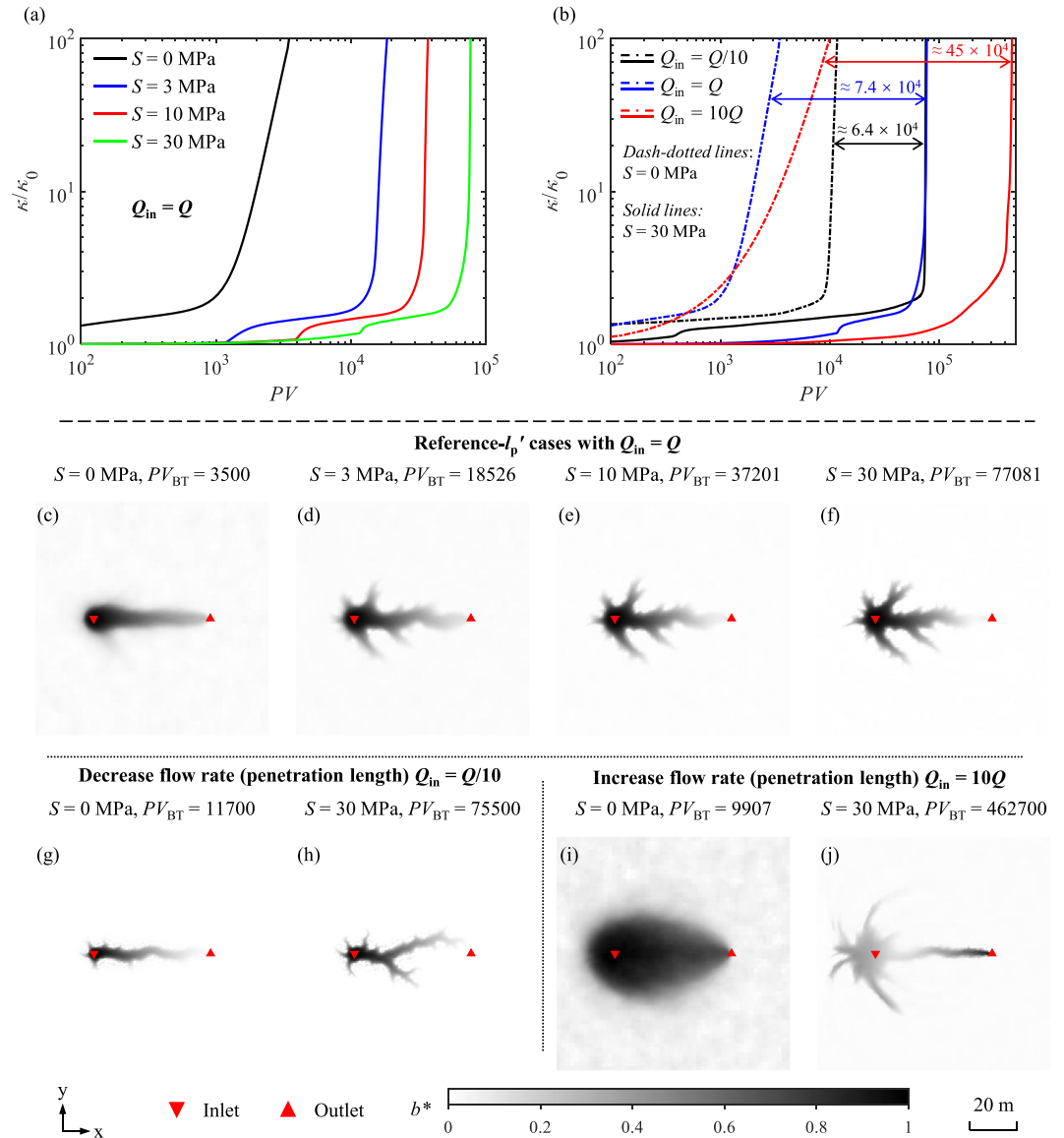


Figure 5. Evolutions of the equivalent permeability ratio κ/κ_0 : (a) reference- l_p' cases ($l_p' \approx 0.2$) under different stress loads, (b) cases with different flow rates (or l_p'). The corresponding distributions of normalized aperture $b^* = [b - \min(b)]/[\max(b) - \min(b)]$ when $\kappa/\kappa_0 = 100$: (c)–(f) reference- l_p' cases (median flow rate: Q , $l_p' \approx 0.2$), (g)–(h) low- l_p' cases (low flow rate: $Q/10$, $l_p' \approx 0.02$), and (i)–(j) high- l_p' cases (high flow rate: $10Q$, $l_p' \approx 2$). A similar trend corresponding to different dissolution rates can be found in Supplementary Information S1 (Fig. S2).

zero-stress scenario. Correspondingly, the evolution of κ/κ_0 displays an abrupt increase like the characteristic wormhole dissolution, in contrast to the more gradual rise of typical uniform dissolution (Figure 5b).

4. Discussion

4.1. Stress-Controlled Shift of Breakthrough Volume PV_{BT}

Our simulation results indicate a notable delay in the formation of large-scale dissolution cavities/conduits within a stressed field-scale fracture compared to an unstressed one and also a significant retardation in their subsequent evolution. This delay occurs due to strong normal compression, which induces reclosure of the large-scale dissolution cavity. This interplay between chemical enlargement and mechanical compaction is similarly observed in the micro-scale dissolution modeling of deformable porous media (Roded et al., 2018) although with

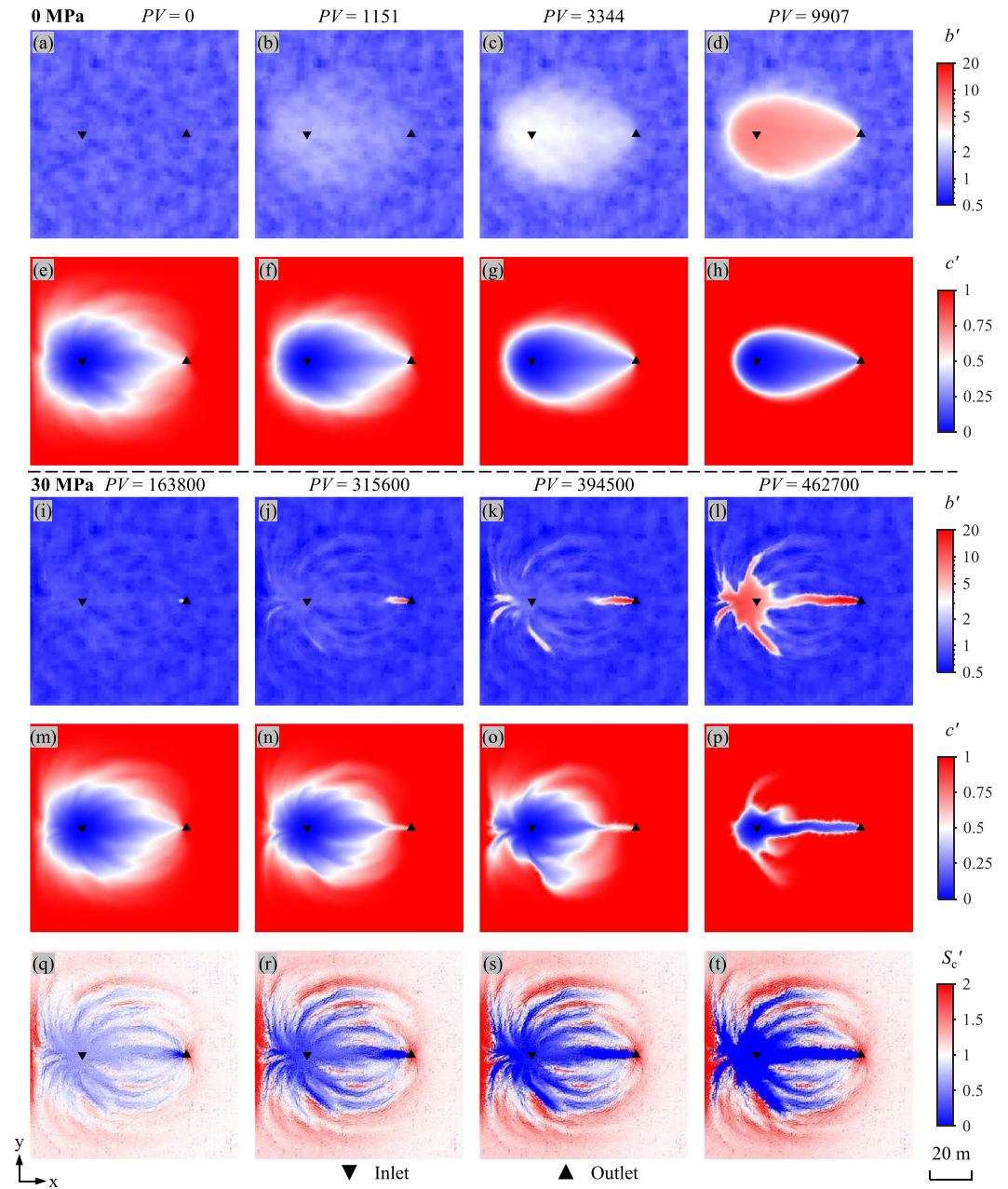


Figure 6. Spatio-temporal evolutions of aperture b' , concentration c' , and local stress S_c' for the high- l_p' cases ($l_p' \approx 2$): a comparison between (a)–(h) $S = 0$ MPa and (i)–(t) $S = 30$ MPa.

a less pronounced difference in breakthrough volume PV_{BT} between stressed and unstressed conditions. This discrepancy may be attributed to the small dissolution vug size in micro-scale simulations. In our simulation, we found that the onset of cavity formation in the initial phase, marked by the deviation of the initial gradual increase of κ/κ_0 , is positively related to the cavity size (or penetration length l_p') (Figure 5a). This implies that larger dissolution areas are more difficult to open under stress load, consistent with experimental observations where larger vugs in carbonates exhibit higher compressibility (greater porosity variation) (Clark & Vanorio, 2016; Yang et al., 2020). To further illustrate the sensitivity of different-sized dissolution cavities to stress loading, we performed additional simulations (see Appendix A and Figure 11 therein) which show that smaller cavities experience less deformation, yielding a larger maximum aperture under load. This indicates that smaller dissolution areas (smaller l_p') produce narrower and less stress-sensitive conduits, thus exhibiting less breakthrough

delay under the same stress condition (Figure 5b). We observe that PV_{BT} for the high- l_p' case is comparable to that of the low- l_p' case at $S = 0$ MPa, but much larger under $S = 30$ MPa due to the delayed early-stage cavity formation (black vs. red lines in Figure 5b). The increase in PV_{BT} by applied stress is positively related to Q_{in} (or l_p') (Figure 5b). Therefore, the optimal condition for a minimum PV_{BT} has to be calibrated under different stress conditions (solid vs. dash-dotted lines in Figure 5b).

4.2. Stress-Controlled Dissolution Fingering

In the low initial penetration regime, as in cases with $l_p' \approx 0.2$ and 0.02 (low flow rate or high dissolution rate), wormhole dissolution occurs. Cheung and Rajaram (2002) found that linear dissolution fingers develop for low heterogeneity of the aperture field, whereas significant branching and winding arise in cases of high heterogeneity. This is attributed to high aperture heterogeneity, which repeatedly divides the primary finger into multiple competing paths at the tip. This phenomenon is remarkably similar to stress-controlled dissolution patterns, where stress load may transition the zero-stress linear dissolution fingers into ramiform patterns characterized by profound branching and winding (Figures 5c–5f). Thus, the essential mechanism is that dissolution under stress is subject to the coexistence of chemically-dissolved cavities and mechanically-induced closures, augmenting the aperture heterogeneity at the tip region and facilitating the splitting of the dissolution front. This is evident from the quantitative analysis based on the correlation dimension of the aperture fields $D_2(b)$, demonstrating that a higher stress load leads to a lower $D_2(b)$ under the same κ/κ_0 (Figure 7a) and thus to more localized aperture enlargement and heterogeneity, which holds for various flow magnitudes. Local strong compaction by stress concentration significantly increases the aperture contrast with local dissolution cavities (Figure 7c vs. Figure 7f, and Fig. S3 in Supporting Information S1), inducing pronounced flow channeling and branching (Figure 7d vs. Figure 7g). Moreover, there is an overall increase in flow throughout the entire preferential flow pathway in the zero-stress case (Figure 7e; Movie S5). In contrast, under stress, the flow at the tip region undergoes strong fluctuations, characterized by frequent alteration between increased and decreased flow in localized areas (Figure 7h; Movie S5). This phenomenon may induce frequent interruptions in the positive feedback loop between flow and dissolution, where dissolution results in localized mechanical weakening and simultaneously generates local stress concentrations in the fringe of the dissolution front (Figures 4i–4l), thus introducing additional resistance along the original pathway. Consequently, this initiates a competitive interplay between mechanical compaction and chemical dissolution, driving the dissolution front to frequently change its preferred penetration direction. This effectively illuminates the impact of stress on the flow in the tip region, leading to the formation of branching and winding patterns. This phenomenon of compaction-induced flow channeling was similarly observed in the non-reactive transport in stressed rough fractures (Kang et al., 2016). The mechanism described above highlights the importance of modeling the effect of local heterogeneity and its evolution driven by coupled HMC processes as captured in our model.

Interestingly, in contrast to the $D_2(b)$ evolutions, the evolutions of $D_2(q)$ with κ/κ_0 are strikingly similar in cases both with and without mechanical effects under the wormhole dissolution regime (see black and blue curves in Figure 7b and Fig. S3 in Supporting Information S1). We further plot the variations of $D_2(b)$ and $D_2(q)$ within several smaller subdomains in Figure 8. It is observed that $D_2(b)$ in the stressed case is always much lower than that in the unstressed case, regardless of the scale. However, stress only leads to more heterogeneous flow at smaller scales, with its effect diminishing progressively as the scale increases. This reveals another important competing mechanism among individual dissolution branches. Although stress induces local flow channeling, these flow channels do not absorb more flow as substantially as in the zero-stress case. Instead, stress significantly suppresses flow enhancement along the preferential flow pathway (note the range of color bars in Figures 7e and 7h), facilitating the development of secondary flow pathways (Roded et al., 2018). In other words, the application of stress not only causes the dissolution front to split into several branches (thus locally increasing flow heterogeneity) but also promotes the sustained growth of dissolution branches due to the decrease of their aperture contrast, globally offsetting the local increase in flow heterogeneity. In contrast, in the zero stress case, we observe a larger aperture contrast among the branches, reflecting a stronger screening effect imposed by primary branches on secondary ones (Sakaguchi et al., 2007). The comparison suggests that stress loading weakens the screening effect by suppressing the positive feedback between flow and dissolution. This highlights the importance of the interplay between small-scale and large-scale flow organizations in dissolution fingering.

In high- l_p' dissolution scenarios, a more complex stress-controlling mechanism occurs, differing significantly from the unstressed uniform dissolution. First, the outlet plays a crucial role, where the localized dissolution area,

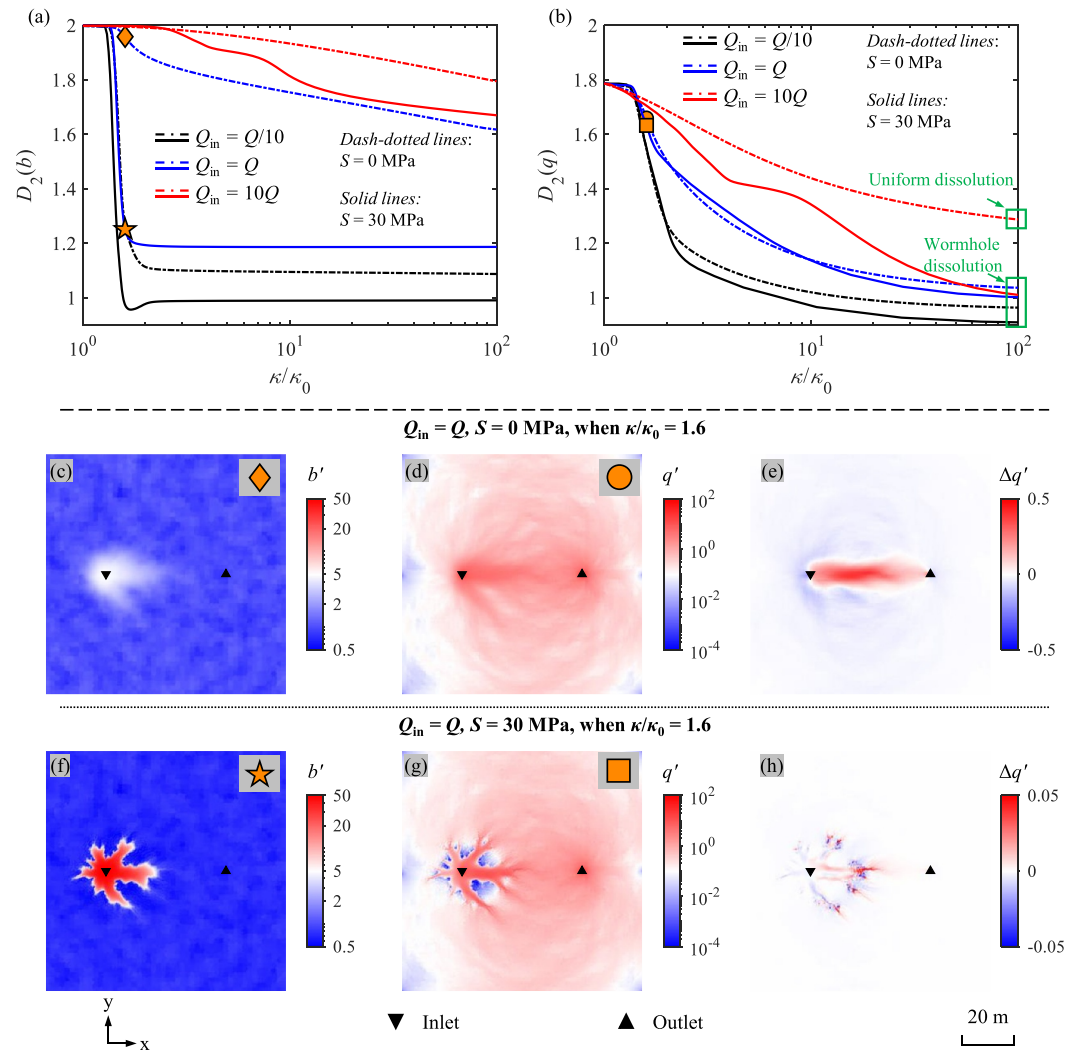


Figure 7. Variations of correlation dimension of (a) the aperture field $D_2(b)$ and (b) the flow field $D_2(q)$ as a function of equivalent permeability ratio κ/κ_0 for the cases with different inlet flow rates. Distributions of (c)–(f) the dimensionless aperture b' , (d)–(g) the local flow rate q' , and (e)–(h) the change of local flow rate $\Delta q'$ compared to that of last time step ($t - 0.1$ years) when $\kappa/\kappa_0 = 1.6$ for reference- I_p' cases. (c)–(e) correspond to when $S = 0$ MPa while (f)–(h) for $S = 30$ MPa. (c) (f) and (d) (g) are the aperture and flow distributions corresponding to the markers in (a) and (b), respectively.

which is stiffer, may lead to earlier initiation of dissolving conduits that penetrate backward toward the inlet. Second, the stress load exacerbates the instability of the dissolution front, resulting from changes in stiffness and redistribution of local stress during dissolution. The previous study without considering mechanical effects indicates that the uniform dissolution extensively homogenizes the heterogeneous medium due to the difference in dissolution rate with varying channel sizes (Roded et al., 2020). In contrast, under stress loading, a distinct splitting of the dissolution front occurs, resulting in branched dissolution fingering. For the stressed high- I_p' case, we found that the variation of $D_2(q)$ as a function of equivalent permeability ratio κ/κ_0 gradually diverges from the unstressed case, finishing with a lower $D_2(q)$ and thus a higher flow channeling (Figure 7b and Fig. S1 in Supporting Information S1). This indicates a qualitative change in the dissolution regime, transitioning from uniform to wormhole dissolution. Also, it implies that stress loads may shift the threshold condition between these two dissolution regimes.

We would like to point out that the stress-induced changes in dissolution patterns captured in our model are much stronger than those in previous micromechanical models (e.g., Ameli et al., 2014). We attribute the difference to two key factors: First, the micromechanical models have only considered the vertical dissolution in non-contact

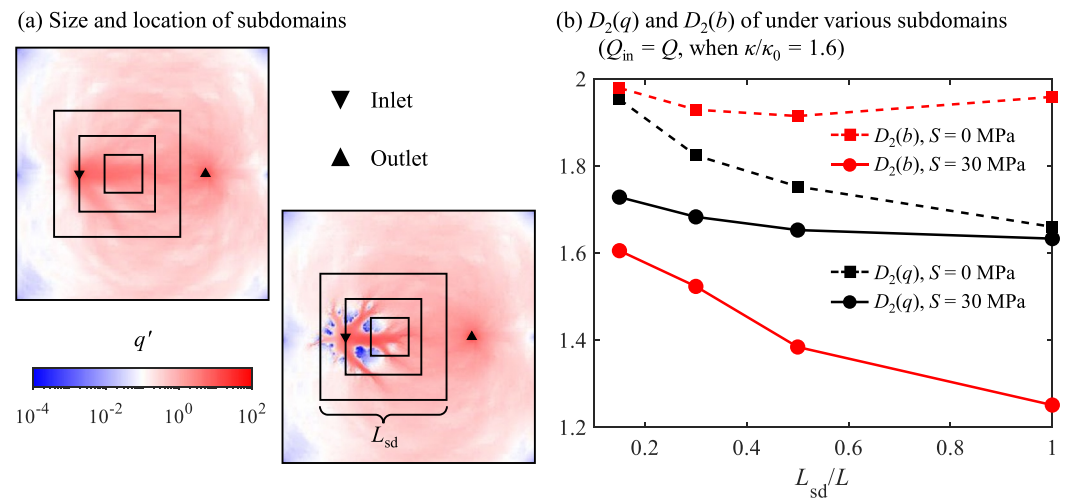


Figure 8. (a) Size and location of subdomains (black boxes). (b) Variations of correlation dimension of the aperture field $D_2(b)$ and the flow field $D_2(q)$ corresponding to different subdomains for the reference- l_p' cases with $S = 0$ MPa and $S = 30$ MPa, when $\kappa/\kappa_0 = 1.6$.

regions and cannot account for the reduction in contact area caused by lateral dissolution of asperities. In contrast, our model could implicitly capture the effects of asperity contact interaction/evolution by considering the changes in the apertures and stiffnesses of local fracture patches. Thus, our model can simulate the process that local fracture patches transition from a “contact mode” to an “open mode”, and eventually merge to form large dissolution cavities over prolonged dissolution, which cannot be captured by the micromechanical models. Second, as noted in Section 4.1, the sensitivity of cavity deformation to stress increases with the cavity size. Our study focuses on large-scale dissolution cavities/conduits (several tens of centimeters or even larger) which exhibit greater stress sensitivity compared to the millimeter-scale dissolution vugs captured in the micromechanical models. Thus, greater stress sensitivity leads to more pronounced changes in dissolution patterns as observed in our study.

4.3. Implications and Perspectives

Our study provides important insights for understanding the formation of diverse karst conduit patterns. As documented in field observations (Palmer, 1991), many epigenic karst systems that develop along bedding planes exhibit single curvilinear passages, whereas hypogenic karst systems are more commonly associated with ramiform morphologies. Our research suggests that stress may be an important factor contributing to the development of ramiform hypogene karst, as many of these systems are located in deep strata. Nevertheless, the formation of hypogenic karst also involves complex hydro-thermal-chemical coupling processes, such as dissolution via the cooling of ascending hot, CO_2 -rich water (Palmer, 1991; Roi Roded et al., 2023). Recent evidence substantiates the widespread occurrence of hypogene karsts globally, with depths down to several kilometers (Klimchouk et al., 2017). Thus, extensive past numerical studies have focused on hypogenic karst genesis (e.g., Andre & Rajaram, 2005; Chaudhuri et al., 2013; Roded et al., 2023), but often overlooked geo-mechanical effects. Roded et al. (2023) recently proposed that confined hydrogeological conditions are prevalent and crucial for hypogene cave formation: the ascending pipe-like thermal flow spreads radially and cools in a confined layer, leading to cave development along bedding planes. In addition, they found that maze dissolution patterns are favored under rapid radial flow, where large chambers form from the merging of adjacent pathways, and the development of the surrounding sparse maze network depends on the distribution of interconnected fracture networks. Our results demonstrate that even within a relatively uniform and well-connected hydraulic conductivity field, narrow channels could develop under significant stress loading, coexisting with large dissolution chambers. In addition, hypogenic karst may entrap deep-seated CO_2 in confined layers and reduce CO_2 release into the atmosphere, which is critical for the carbon cycle (Roded et al., 2023). We suggest that geo-mechanical effects may further impede the propagation of the CO_2 -rich dissolution front. Overlooking the interaction between chemical dissolution and mechanical deformation may lead to a substantial underestimation of the time required to form extensive caves or the time for CO_2 to reach escape exits. Our work also has

implications for various engineering applications. For instance, determining the optimal acid injection rate during reservoir acidization may need to consider geomechanical effects (Xu et al., 2021). Temperature variations and injection conditions of chemical non-equilibrium may induce mineral dissolution/precipitation during geothermal development where the chemical-mechanical coupling could affect the system efficiency (Song et al., 2023).

The findings of this study pave the way for investigating complex HMC processes in field-scale fractures which requires continued research efforts. First, we found that simultaneous reduction and concentration of local stress occur at the center and fringe of the dissolution area, respectively. In addition to the mechanical closure addressed in this work, pressure solution and mineral precipitation may occur at stress-concentration regions, further obstructing the flow space and reducing the aperture (Yasuhara et al., 2006). This implies that pressure solution may not only be activated by environmental condition changes (i.e., pore pressure reduction or temperature increase) (Lu et al., 2018; Yasuhara et al., 2006), but also by reactive transport itself involving local dissolution and aperture enlargement. We postulate that pressure solution may further inhibit the permeability enhancement and impact the dissolution patterns. The evaluation of the pressure solution effect may be performed based on a simplification of the asperity shape (J. Liu et al., 2006). Second, shear dilation effects will be explored in our future work. We observed that dissolution may lead to local stiffness weakening and local stress reduction, potentially increasing the likelihood of triggering shear slip and seismicity (Galloway et al., 2018). Certainly, some complicated mechanisms may be involved, such as mineral decomposition, melting, and so, leading to a sharp decrease in the friction coefficient (Rattez & Veveakis, 2020).

5. Conclusions

We presented a new coupled HMC model for simulating the dissolution process in a stressed hectometer-scale fracture. We found that stress retards the permeability increase to an extent positively related to the dimensionless penetration length l_p' . Unlike dissolution under a zero-stress condition, where flow rapidly converges into a preferential pathway, we observed that branched dissolution fronts emerge in stressed scenarios. At low l_p' , stress promotes local flow focusing and the formation of multiple persistently growing dissolution branches. Hence, the level of global flow heterogeneity does not seem to vary much. At high l_p' , stress causes the dissolution front to split, qualitatively distinct from the uniform dissolution under zero stress. The dissolution regime transitions to wormhole dissolution, with localized dissolving conduits originating from remote stiffer regions and converging toward the inlet. Our research findings improve the fundamental understanding of natural karst genesis and also have important implications for various engineering applications such as geothermal development and reservoir acidization.

Appendix A: Model Verification for the Deformation of Field-Scale Cavities

As shown in Figure A1, we consider a 100^3 m^3 rock cube where a large horizontal fracture with cavities is placed in the middle. Here, two types of field-scale cavities are considered to verify the interaction of adjacent contacts/cavities: a single cavity (Figures A1a and A1b) and a dual-cavity combination (Figures A1c and A1d). We compare two representations of cavities: (a) a lower-dimensional surface with an implicit gap distribution and (b) a three-dimensional cavity structure with an explicit gap distribution (Figures A1a and A1c).

To mimic the aperture enlargement due to dissolution, we employ a Gaussian function to describe an initial gap distribution, where the z -coordinates of the upper and lower surfaces follow:

$$z(r) = \pm b_{\max} e^{-\frac{r^2}{2\zeta^2}}, \quad (\text{A1})$$

where b_{\max} is the maximum of the half gap, r is the distance to the cavity center and ζ is the standard deviation of the function. For the single-cavity case, the gap distribution is mapped on a circular fracture with a 30 m radius and centered at (50, 50, 0) (Figure A1b). We assume a cavity size formed during incipient karst which can be $2b_{\max} = 20 \text{ mm}$. For the dual-cavity case, the gap distribution combines two Gaussian functions, that is, $z = \max(z_1, z_2)$ for the upper surface and $z = \min(z_1, z_2)$ for the lower surface (Figure A1d). The two circular fractures, each with a 30 m radius, are centered respectively at (45, 50, 0) and (55, 50, 0). The maximum gap size of the left cavity ($2b_{\max 1}$) is 30 mm while that of the right one ($2b_{\max 2}$) is 20 mm (Figures A1c and A1d). Taking $\zeta = 6.67 \text{ m}$, the initial gap distributions are shown in Figures A1b and A1d, respectively. Here, the normal stiffness is

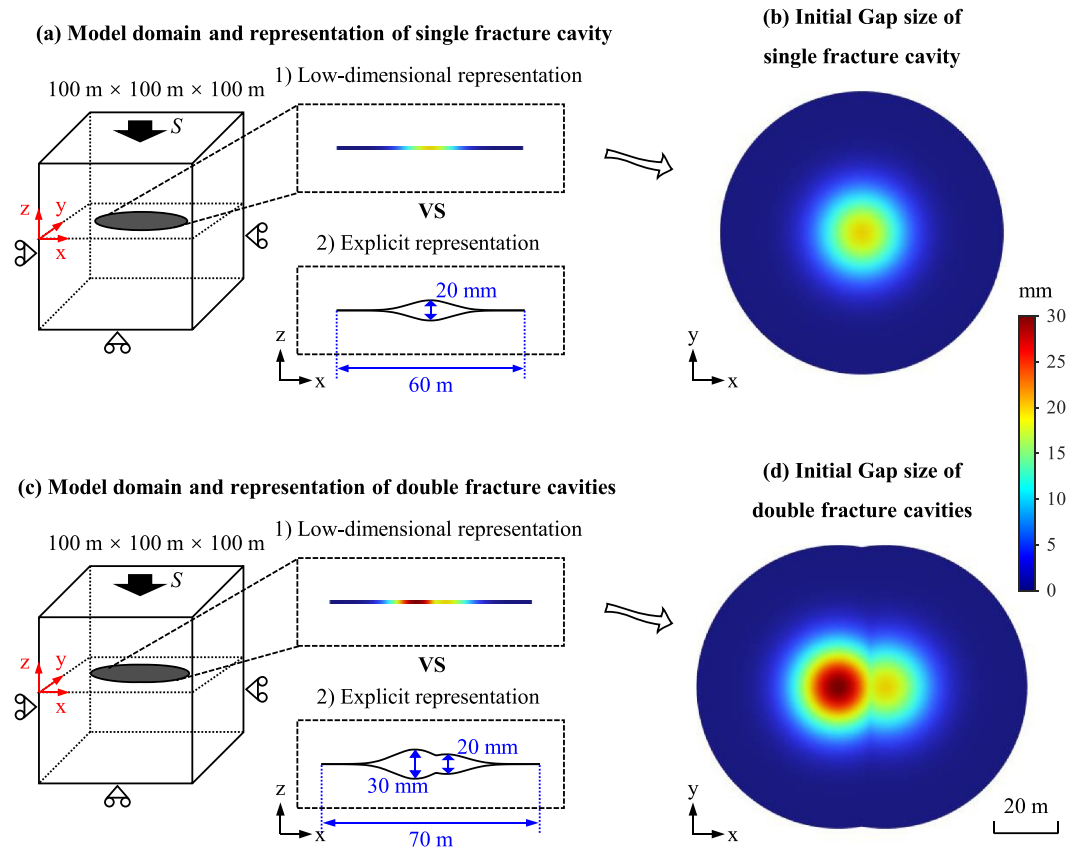


Figure A1. (a) Model domain and two representations of fracture gap for the single-cavity case: (1) a lower-dimensional surface with an implicit gap distribution and (2) a three-dimensional cavity structure with an explicit gap distribution. (b) Distribution of initial gap size for the single-cavity case. (c) and (d) Corresponding model setup for the dual-cavity case.

simplified as a constant, $K_n = 20$ MPa/mm. Young's modulus, Poisson's ratio, and density of the rock matrix are the same as those defined in Table 1.

Figure A2 shows the distributions of the local stress and the remaining gap size under normal compressive loads of $S = 15$ MPa. The simulation results show that our lower-dimensional model agrees perfectly with the explicit model. In the single-cavity case, the majority of the fracture surface is in contact, although the central high-gap region (indicative of the dissolution hotspot) closes partially and remains open. Due to the loss of contact area, the edge of the open area carries the extra load, resulting in stress concentration (with the local stress exceeding 15 MPa) (Figures A2a and A2b). This implies stiffness weakening and stress reduction at the dissolution hotspot as well as stress concentration at its fringes, in agreement with previous experimental observations (e.g., Cha & Santamarina, 2016). In the dual-cavity case, we further confirm that our lower-dimensional model can capture the interaction of adjacent cavities. The lower-dimensional model remains consistent with the explicit model. Affected by the deformation of the larger cavity on the left side, the remaining gap size of the right cavity is reduced compared to the single-cavity case. Meanwhile, the stress concentration on the left side of the whole fracture is stronger than on the right side.

Figure A3 further presents a sensitivity analysis of the impact of stress on cavities of different sizes. Here, we fix the maximum cavity aperture at $2b_{\max} = 20$ mm and simulate the deformation under a 15 MPa stress load for cavities with different lateral radii (denoted by ζ). The results show that the smaller the lateral size of the cavity, the less deformable it is, resulting in a larger aperture under the applied load. This reveals that if the dissolution area is smaller (corresponding to a smaller l_p), the dissolution conduits are narrower, and consequently, the sensitivity of these dissolution conduits to stress is less.

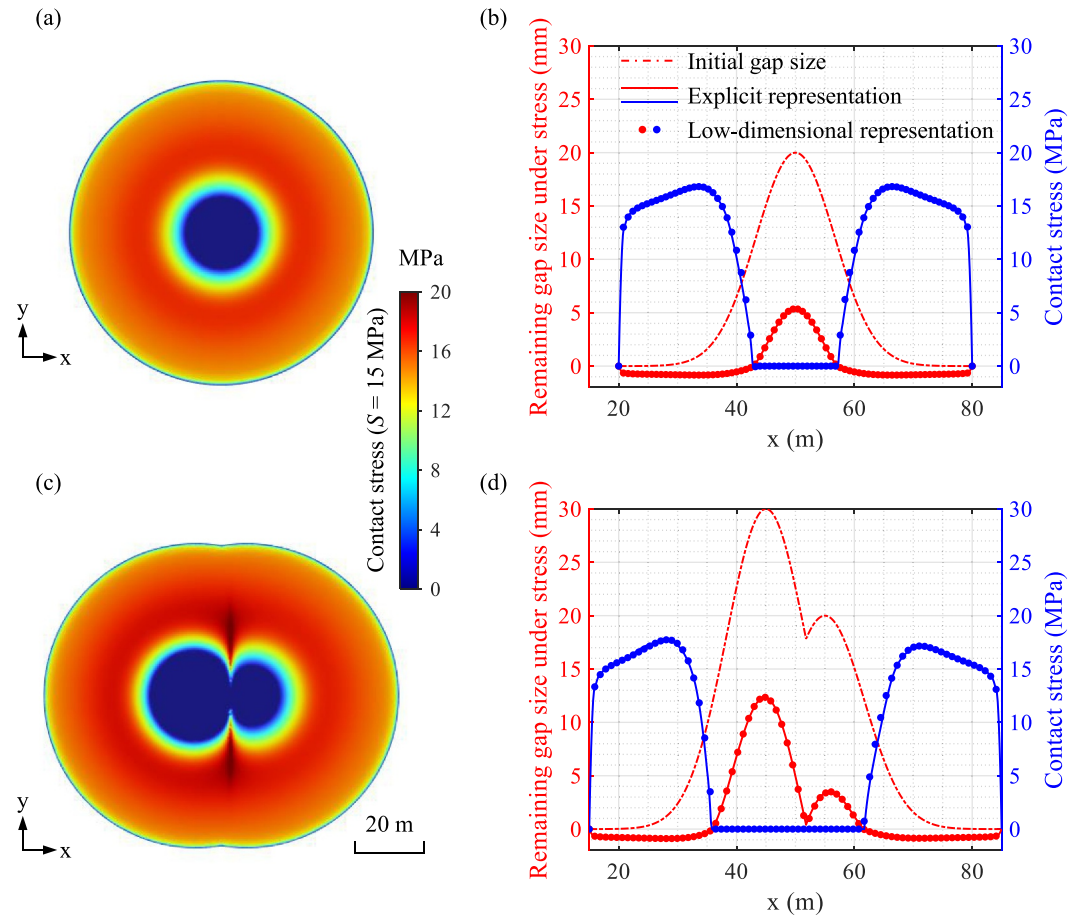


Figure A2. Distribution of local stress when the applied normal compressive load S is 15 MPa in (a) single-cavity case and (c) dual-cavity case. Corresponding distributions of the initial gap size, remaining gap size, and local stress across the fracture (in the cross-section along $y = 50$ m) under normal compressive loads $S = 15$ MPa, in (b) single-cavity case and (d) dual-cavity case.

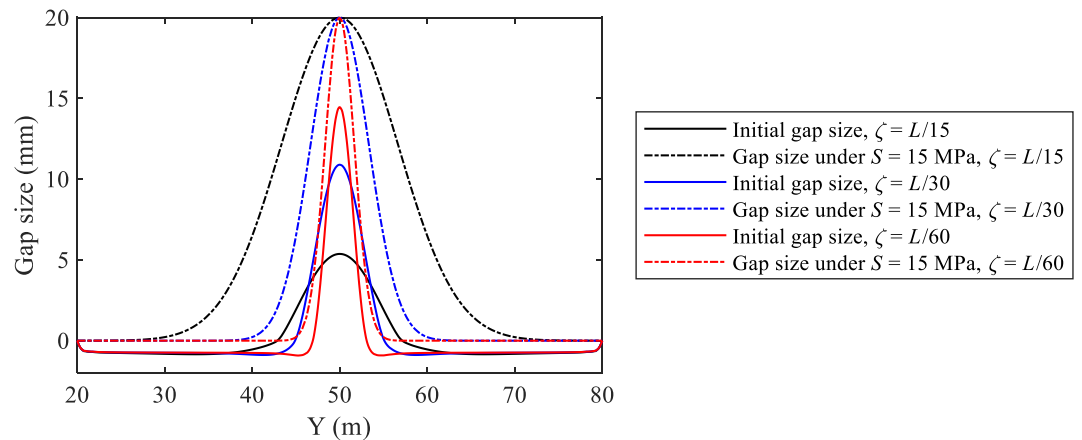


Figure A3. Distributions of the initial gap size and remaining gap size when the applied normal compressive load S is 15 MPa in the single-cavity scenario, corresponding to the cases of different cavity radii (denoted by ζ). L is the domain size, that is, 100 m.

Conflict of Interest

The authors declare no conflicts of interest relevant to this study.

Data Availability Statement

Supporting Information includes Figures S1–S3 and Movies S1–S5 in Supporting Information S1. The data generated by this study are available at (Jiang et al., 2024).

Acknowledgments

C.J. is supported by the China Scholarship Council (CSC) from the Ministry of Education of P.R. China (202006450151). X.W. is grateful for the support from National Natural Science Foundation of China (42102300, 42372300), Science & Technology Department of Sichuan Province (2021ZYCD004, 2022YFSY0008) and State Key Laboratory of Geohazard Prevention and Geoenvironment Protection (SKLGP2022K024).

References

- Ameli, P., Elkhouri, J. E., Morris, J. P., & Detwiler, R. L. (2014). Fracture permeability alteration due to chemical and mechanical processes: A coupled high-resolution model. *Rock Mechanics and Rock Engineering*, 47(5), 1563–1573. <https://doi.org/10.1007/s00603-014-0575-z>
- Andre, B. J., & Rajaram, H. (2005). Dissolution of limestone fractures by cooling waters: Early development of hypogene karst systems. *Water Resources Research*, 41(1). <https://doi.org/10.1029/2004wr003331>
- Bandis, S. C., Lumsden, A. C., & Barton, N. R. (1983). Fundamentals of rock joint deformation. *International Journal of Rock Mechanics and Mining Sciences & Geomechanics Abstracts*, 20(6), 249–268. [https://doi.org/10.1016/0148-9062\(83\)90595-8](https://doi.org/10.1016/0148-9062(83)90595-8)
- Bonnet, E., Bour, O., Odling, N. E., Davy, P., Main, I., Cowie, P., & Berkowitz, B. (2001). Scaling of fracture systems in geological media. *Reviews of Geophysics*, 39(3), 347–383. <https://doi.org/10.1029/1999RG000074>
- Brown, S. R. (1995). Simple mathematical model of a rough fracture. *Journal of Geophysical Research*, 100(B4), 5941–5952. <https://doi.org/10.1029/94jb03262>
- Cha, M., & Santamarina, J. C. (2016). Hydro-chemo-mechanical coupling in sediments: Localized mineral dissolution. *Geomechanics for Energy and the Environment*, 7, 1–9. <https://doi.org/10.1016/j.gete.2016.06.001>
- Chaudhuri, A., Rajaram, H., & Viswanathan, H. (2013). Early-stage hypogene karstification in a mountain hydrologic system: A coupled thermohydrochemical model incorporating buoyant convection. *Water Resources Research*, 49(9), 5880–5899. <https://doi.org/10.1002/wrcr.20427>
- Cheung, W., & Rajaram, H. (2002). Dissolution finger growth in variable aperture fractures: Role of the tip-region flow field. *Geophysical Research Letters*, 29(22), 32–41. <https://doi.org/10.1029/2002gl015196>
- Clark, A. C., & Vanorio, T. (2016). The rock physics and geochemistry of carbonates exposed to reactive brines. *Journal of Geophysical Research: Solid Earth*, 121(3), 1497–1513. <https://doi.org/10.1002/2015jb012445>
- De Dreuzy, J.-R., Méheust, Y., & Pichot, G. (2012). Influence of fracture scale heterogeneity on the flow properties of three-dimensional discrete fracture networks (DFN). *Journal of Geophysical Research*, 117(B11). <https://doi.org/10.1029/2012jb009461>
- Detwiler, R. L. (2008). Experimental observations of deformation caused by mineral dissolution in variable-aperture fractures. *Journal of Geophysical Research*, 113(B8). <https://doi.org/10.1029/2008jb005697>
- Detwiler, R. L., Glass, R. J., & Bourcier, W. L. (2003). Experimental observations of fracture dissolution: The role of Peclet number on evolving aperture variability. *Geophysical Research Letters*, 30(12). <https://doi.org/10.1029/2003gl017396>
- Dreybrodt, W., & Gabrovšek, F. (2019). Dynamics of wormhole formation in fractured limestones. *Hydrology and Earth System Sciences*, 23(4), 1995–2014. <https://doi.org/10.5194/hess-23-1995-2019>
- Elkhouri, J. E., Ameli, P., & Detwiler, R. L. (2013). Dissolution and deformation in fractured carbonates caused by flow of CO₂-rich brine under reservoir conditions. *International Journal of Greenhouse Gas Control*, 16, S203–S215. <https://doi.org/10.1016/j.ijggc.2013.02.023>
- Galloway, E., Hauck, T., Corlett, H., Pană, D., & Schultz, R. (2018). Faults and associated karst collapse suggest conduits for fluid flow that influence hydraulic fracturing-induced seismicity. *Proceedings of the National Academy of Sciences*, 115(43), E10003–E10012. <https://doi.org/10.1073/pnas.1807549115>
- Hanna, R. B., & Rajaram, H. (1998). Influence of aperture variability on dissolutional growth of fissures in Karst Formations. *Water Resources Research*, 34(11), 2843–2853. <https://doi.org/10.1029/98WR01528>
- Hyman, J. D., Navarre-Sitchler, A., Andrews, E., Sweeney, M. R., Karra, S., Carey, J. W., & Viswanathan, H. S. (2022). A geo-structurally based correction factor for apparent dissolution rates in fractured media. *Geophysical Research Letters*, 49(15), e2022GL099513. <https://doi.org/10.1029/2022gl099513>
- Jiang, C., Wang, X., Lei, Q., Liu, L., Song, G., & Jourde, H. (2024). Evidence of stress control on dissolution cavity growth along heterogeneous field-scale fractures from coupled hydro-mechanical-chemical modeling (version 2) [Dataset]. *Zenodo*. <https://zenodo.org/records/14036861>
- Jiang, C., Wang, X., Pu, S., & Jourde, H. (2022). Incipient karst generation in jointed layered carbonates: Insights from three-dimensional hydro-chemical simulations. *Journal of Hydrology*, 610, 127831. <https://doi.org/10.1016/j.jhydrol.2022.127831>
- Jiang, C., Wang, X., Zhang, F., Deng, K., & Lei, Q. (2022). Fracture activation and induced seismicity during long-term heat production in fractured geothermal reservoirs. *Rock Mechanics and Rock Engineering*, 55(8), 5235–5258. <https://doi.org/10.1007/s00603-022-02882-z>
- Kang, P. K., Brown, S., & Juanes, R. (2016). Emergence of anomalous transport in stressed rough fractures. *Earth and Planetary Science Letters*, 454, 46–54. <https://doi.org/10.1016/j.epsl.2016.08.033>
- Klimchouk, A., Palmer, A. N., De Waele, J., Auler, A. S., & Audra, P. (2017). *Hypogene karst regions and caves of the world*. Springer.
- Lang, P., Paluszny, A., & Zimmerman, R. (2015). Hydraulic sealing due to pressure solution contact zone growth in siliciclastic rock fractures. *Journal of Geophysical Research: Solid Earth*, 120(6), 4080–4101. <https://doi.org/10.1002/2015jb011968>
- Lei, Q., & Barton, N. (2022). On the selection of joint constitutive models for geomechanics simulation of fractured rocks. *Computers and Geotechnics*, 145, 104707. <https://doi.org/10.1016/j.compgeo.2022.104707>
- Lei, Q., Wang, X., Xiang, J., & Latham, J.-P. (2017). Polyaxial stress-dependent permeability of a three-dimensional fractured rock layer. *Hydrogeology Journal*, 25(8), 2251–2262. <https://doi.org/10.1007/s10040-017-1624-y>
- Li, B., Cui, X., Zou, L., & Cvetkovic, V. (2021). On the relationship between normal stiffness and permeability of rock fractures. *Geophysical Research Letters*, 48(20), e2021GL095593. <https://doi.org/10.1029/2021gl095593>
- Liu, J., Sheng, J., Polak, A., Elsworth, D., Yasuhara, H., & Grader, A. (2006). A fully-coupled hydrological–mechanical–chemical model for fracture sealing and preferential opening. *International Journal of Rock Mechanics and Mining Sciences*, 43(1), 23–36. <https://doi.org/10.1016/j.ijrmms.2005.04.012>

- Liu, L., Huang, Z., Yao, J., Lei, Q., Di, Y., Wu, Y.-S., et al. (2021). Simulating two-phase flow and geomechanical deformation in fractured karst reservoirs based on a coupled hydro-mechanical model. *International Journal of Rock Mechanics and Mining Sciences*, 137, 104543. <https://doi.org/10.1016/j.ijrmms.2020.104543>
- Lu, R., Nagel, T., Shao, H., Kolditz, O., & Shao, H. (2018). Modeling of dissolution-induced permeability evolution of a granite fracture under crustal conditions. *Journal of Geophysical Research: Solid Earth*, 123(7), 5609–5627. <https://doi.org/10.1029/2018jb015702>
- Neuman, S. P. (1987). Stochastic continuum representation of fractured rock permeability as an alternative to the REV and fracture network concepts. In *ARMA US rock Mechanics/Geomechanics Symposium* (p. ARMA-87). ARMA.
- Ogata, S., Yasuhara, H., Kinoshita, N., Cheon, D.-S., & Kishida, K. (2018). Modeling of coupled thermal-hydraulic-mechanical-chemical processes for predicting the evolution in permeability and reactive transport behavior within single rock fractures. *International Journal of Rock Mechanics and Mining Sciences*, 107, 271–281. <https://doi.org/10.1016/j.ijrmms.2018.04.015>
- Palmer, A. N. (1991). Origin and morphology of limestone caves. *Geological Society of America Bulletin*, 103(1), 1–21. [https://doi.org/10.1130/0016-7606\(1991\)103<0001:oamolc>2.3.co;2](https://doi.org/10.1130/0016-7606(1991)103<0001:oamolc>2.3.co;2)
- Pandey, S., Vishal, V., & Chaudhuri, A. (2018). Geothermal reservoir modeling in a coupled thermo-hydro-mechanical-chemical approach: A review. *Earth-Science Reviews*, 185, 1157–1169. <https://doi.org/10.1016/j.earscirev.2018.09.004>
- Petrovitch, C. L., Nolte, D. D., & Pyrak-Nolte, L. J. (2013). Scaling of fluid flow versus fracture stiffness. *Geophysical Research Letters*, 40(10), 2076–2080. <https://doi.org/10.1002/grl.50479>
- Pyrak-Nolte, L. J., & Morris, J. P. (2000). Single fractures under normal stress: The relation between fracture specific stiffness and fluid flow. *International Journal of Rock Mechanics and Mining Sciences*, 37(1–2), 245–262. [https://doi.org/10.1016/S1365-1609\(99\)00104-5](https://doi.org/10.1016/S1365-1609(99)00104-5)
- Pyrak-Nolte, L. J., & Nolte, D. D. (2016). Approaching a universal scaling relationship between fracture stiffness and fluid flow. *Nature Communications*, 7(1), 10663. <https://doi.org/10.1038/ncomms10663>
- Ratteez, H., & Veveakis, M. (2020). Weak phases production and heat generation control fault friction during seismic slip. *Nature Communications*, 11(1), 350. <https://doi.org/10.1038/s41467-019-14252-5>
- Roded, R., Aharonov, E., Frumkin, A., Weber, N., Lazar, B., & Szymczak, P. (2023). Cooling of hydrothermal fluids rich in carbon dioxide can create large karst cave systems in carbonate rocks. *Communications Earth & Environment*, 4(1), 465. <https://doi.org/10.1038/s43247-023-01082-z>
- Roded, R., Aharonov, E., Holtzman, R., & Szymczak, P. (2020). Reactive flow and homogenization in anisotropic media. *Water Resources Research*, 56(12), e2020WR027518. <https://doi.org/10.1029/2020wr027518>
- Roded, R., Paredes, X., & Holtzman, R. (2018). Reactive transport under stress: Permeability evolution in deformable porous media. *Earth and Planetary Science Letters*, 493, 198–207. <https://doi.org/10.1016/j.epsl.2018.04.041>
- Rutqvist, J., Wu, Y.-S., Tsang, C.-F., & Bodvarsson, G. (2002). A modeling approach for analysis of coupled multiphase fluid flow, heat transfer, and deformation in fractured porous rock. *International Journal of Rock Mechanics and Mining Sciences*, 39(4), 429–442. [https://doi.org/10.1016/S1365-1609\(02\)00022-9](https://doi.org/10.1016/S1365-1609(02)00022-9)
- Sakaguchi, H., Kishinawa, K., Katsuki, K., & Honjo, H. (2007). Simple model for competitive dynamics among dendritic sidebranches. *Physical Review E: Statistical, Nonlinear, and Soft Matter Physics*, 75(2), 021606. <https://doi.org/10.1103/physreve.75.021606>
- Salimzadeh, S., & Nick, H. (2019). A coupled model for reactive flow through deformable fractures in enhanced geothermal systems. *Geothermics*, 81, 88–100. <https://doi.org/10.1016/j.geothermics.2019.04.010>
- Song, G., Shi, Y., Xu, F., Song, X., Li, G., Wang, G., & Lv, Z. (2023). The magnitudes of multi-physics effects on geothermal reservoir characteristics during the production of enhanced geothermal system. *Journal of Cleaner Production*, 434, 140070. <https://doi.org/10.1016/j.jclepro.2023.140070>
- Song, G., Song, X., Xu, F., Li, G., Shi, Y., & Ji, J. (2022). Contributions of thermo-poroelastic and chemical effects to the production of enhanced geothermal system based on thermo-hydro-mechanical-chemical modeling. *Journal of Cleaner Production*, 377, 134471. <https://doi.org/10.1016/j.jclepro.2022.134471>
- Starchenko, V., & Ladd, A. J. (2018). The development of wormholes in laboratory-scale fractures: Perspectives from three-dimensional simulations. *Water Resources Research*, 54(10), 7946–7959. <https://doi.org/10.1029/2018wr022948>
- Steiger, M., Charola, A. E., & Sterflinger, K. (2011). Weathering and deterioration. *Stone in Architecture: Properties, Durability*, 227–316. https://doi.org/10.1007/978-3-642-14475-2_4
- Szymczak, P., & Ladd, A. J. (2009). Wormhole formation in dissolving fractures. *Journal of Geophysical Research*, 114(B6), B06203. <https://doi.org/10.1029/2008JB006122>
- Szymczak, P., & Ladd, A. J. (2011). The initial stages of cave formation: Beyond the one-dimensional paradigm. *Earth and Planetary Science Letters*, 301(3–4), 424–432. <https://doi.org/10.1016/j.epsl.2010.10.026>
- Wang, T., Hu, R., Yang, Z., Zhou, C.-X., Chen, Y.-F., & Zhou, C.-B. (2022). Transitions of dissolution patterns in rough fractures. *Water Resources Research*, 58(1), e2021WR030456. <https://doi.org/10.1029/2021wr030456>
- Wang, X., Aliouache, M., Wang, Y., Lei, Q., & Jourde, H. (2021). The role of aperture heterogeneity in incipient karst evolution in natural fracture networks: Insights from numerical simulations. *Advances in Water Resources*, 156, 104036. <https://doi.org/10.1016/j.advwatres.2021.104036>
- Wang, X., Lei, Q., Lonergan, L., Jourde, H., Gosselin, O., & Cosgrove, J. (2017). Heterogeneous fluid flow in fractured layered carbonates and its implication for generation of incipient karst. *Advances in Water Resources*, 107, 502–516. <https://doi.org/10.1016/j.advwatres.2017.05.016>
- Witherspoon, P. A., Wang, J. S., Iwai, K., & Gale, J. E. (1980). Validity of cubic law for fluid flow in a deformable rock fracture. *Water Resources Research*, 16(6), 1016–1024. <https://doi.org/10.1029/wr016i006p01016>
- Wong, L. N. Y., Maruvanchery, V., & Liu, G. (2016). Water effects on rock strength and stiffness degradation. *Acta Geotechnica*, 11(4), 713–737. <https://doi.org/10.1007/s11440-015-0407-7>
- Xia, L., Zheng, Y., & Yu, Q. (2016). Estimation of the REV size for blockiness of fractured rock masses. *Computers and Geotechnics*, 76, 83–92. <https://doi.org/10.1016/j.compgeo.2016.02.016>
- Xu, H., Cheng, J., Zhao, Z., Lin, T., Liu, G., & Chen, S. (2021). Coupled thermo-hydro-mechanical-chemical modeling on acid fracturing in carbonate geothermal reservoirs containing a heterogeneous fracture. *Renewable Energy*, 172, 145–157. <https://doi.org/10.1016/j.renene.2021.03.023>
- Yang, Y., Tao, L., Yang, H., Iglauer, S., Wang, X., Askari, R., et al. (2020). Stress sensitivity of fractured and vuggy carbonate: An X-Ray computed tomography analysis. *Journal of Geophysical Research: Solid Earth*, 125(3), e2019JB018759. <https://doi.org/10.1029/2019jb018759>

- Yasuhara, H., Kinoshita, N., Ohfuji, H., Takahashi, M., Ito, K., & Kishida, K. (2015). Long-term observation of permeability in sedimentary rocks under high-temperature and stress conditions and its interpretation mediated by microstructural investigations. *Water Resources Research*, 51(7), 5425–5449. <https://doi.org/10.1002/2014wr016427>
- Yasuhara, H., Polak, A., Mitani, Y., Grader, A. S., Halleck, P. M., & Elsworth, D. (2006). Evolution of fracture permeability through fluid–rock reaction under hydrothermal conditions. *Earth and Planetary Science Letters*, 244(1–2), 186–200. <https://doi.org/10.1016/j.epsl.2006.01.046>